STUDIA UBB CHEMIA, LXXI, 2, 2026 (p. 65-85)
(RECOMMENDED CITATION)
DOI:10.24193/subbchem.2026.2.04

GREEN SYNTHESIS AND STRUCTURAL CHARACTERIZATION OF IRON OXIDE NANOPARTICLES FROM *ROBINIA PSEUDOACACIA* L. FRUITS FOR DYE REMOVAL FROM AQUEOUS SOLUTIONS

Semra DEMIR[a], Bülent AKAR[b,*], Cemalettin BALTACI[b]

ABSTRACT. In this study, iron oxide nanoparticles were produced and characterized using a green synthesis method with *Robinia pseudoacacia* fruits. The structural and functional properties of the nanoparticles were investigated using XRD, TEM/EDX, and FTIR analyses. The results indicated that the produced iron oxide nanoparticles had nanoscale particle sizes and exhibited a poorly crystalline (predominantly amorphous) structure according to XRD analysis. The comparative adsorption performance of the synthesized FeONPs and fruit powder in the removal of malachite green (MG), phenol red (PR) and methylene blue (MB) from aqueous solutions was evaluated. According to the results, the adsorption capacity followed the order MB> MG > PR. FeONPs exhibited consistently higher Q_e values across all dye systems compared to the fruit powder. High removal efficiencies were obtained at low and moderate initial concentrations, while increasing the adsorbent dose enhanced the overall removal but resulted in a reduction in the adsorption capacity per unit mass. The obtained findings indicate that biosynthesized iron oxide nanoparticles can be used as an efficient and environmentally friendly adsorbent for eliminating environmental pollutants.

Keywords: *green synthesis, fruit extract, iron oxide nanoparticles, Robinia pseudoacacia, dye removal*

[a] *Gümüşhane University, Graduate Education Institute, Department of Biotechnology, 29000, Gümüşhane, Türkiye*
[b] *Gümüşhane University, Faculty of Engineering and Natural Sciences, Department of Food Engineering, 29000, Gümüşhane, Türkiye*
* *Corresponding author: akarblnt@gmail.com*

INTRODUCTION

When it comes to the management of environmentally polluted areas, since the pollutant removal of from contaminated environments is generally a process that involves high costs due to technical requirements, preventive strategies aimed at avoiding the environmental contamination and natural resources from the outset are much more sustainable and effective. However, pollutants originating largely from intensive human activities enter the air, water, and soil and accumulate, creating stress on ecosystems, reducing biodiversity, decreasing soil fertility, and leading to crop losses. In addition, the transfer of these pollutants across the food chain poses various threats to other organisms and humans [1]. The increase in environmental pollution has required the development of appropriate methods for remediation of pollution sources from affected environments. The elimination of contaminants from the environment through organisms is referred to as bioremediation. The primary aim of this technology is to reduce or remove pollution [2]. Phytoremediation, defined as the elimination of pollutants from contaminated soil, air, and water using plants, is a type of bioremediation. This approach involves the use of plants together with rhizosphere microorganisms to eliminate, transform, or accumulate chemical compounds present in groundwater, surface water, soil, sediment, and the atmosphere [3-4]. Recently, studies using innovative approaches have increasingly targeted the reduction of pollution levels. Nanotechnology, with applications in a wide range of scientific and industrial fields, is also attracting growing attention in environmental remediation [5]. Notably, the production of nanosized particles using chemical and physical methods has long been recognized as a conventional approach [6-7]. However, due to these disadvantages, biological synthesis (green synthesis) has emerged in recent years as a simpler, lower-cost, and environmentally friendly alternative [8]. Indeed, research on biologically synthesized nanoparticles using yeasts, bacteria, algae and plants, have seen a significant increase in the last decade compared to chemical and physical methods [9-10]. Biosynthesis studies often include metal and metal oxide nanoparticles. Owing to their unique biological, physicochemical, magnetic, and optical characteristics, these nanoparticles have attracted considerable scientific interest [11]. In this context, the ability of plants to reduce metal ions is one of the key features of biological (green) synthesis processes. Plant extracts are among the most widely used natural reducing agents due to their lower cost, easier availability and high biocompatibility. In particular, the polyphenols, terpenoids, glutathione, carotenoids, and glucosinolates found in these extracts are environmentally

friendly biomolecules that contribute to the reduction of metal ions and the stabilization of nanoparticles [12]. One significant application area for environmentally friendly approaches is the remediation of water pollution. As water pollution is a serious global environmental problem, research into effective treatment strategies is intensifying. Bioremediation processes are therefore receiving increasing attention as a means of removing organic pollutants and heavy metals from aqueous solutions [13]. Bioremediation of dyes in wastewater is an effective method of treating textile waste, offering advantages over traditional techniques. Dyes are classified as hazardous pollutants by various international environmental agencies, including the US Environmental Protection Agency (EPA). Due to their carcinogenic properties, even low concentrations of dyes in water can have serious negative environmental and ecological impacts [14].

In bioremediation studies, plant-derived materials are commonly used as effective, sustainable and economical absorbents for removing synthetic dyes from water [15]. In this study, the fruits of *Robinia pseudoacacia* L., belonging to the Fabaceae family, and iron oxide nanoparticles obtained from these extracts, were characterized and their capacity to remove polluting dyes from water was determined. The *R. pseudoacacia* tree is adaptable to environmental stress and has high ecological and economic value. It is therefore widely used as an ornamental plant and for landscaping purposes in Türkiye and many others around the world [16]. The chemical composition and biological activities of *R. pseudoacacia* have been studied [17-19]. These studies have revealed that the species exhibits significant biological activity. Although other plant species and metal oxides may possess the potential for high dye-removal efficiency, many of these alternatives are not practical for dye remediation applications because of their high cost and limited availability. Therefore, the use of *R. pseudoacacia* fruit as an economical and readily accessible biomass, together with iron as a low-cost and environmentally benign metal, forms the main basis for their selection in this study. This study aims to synthesize iron oxide nanoparticles through a green approach using fruit extracts of *R. pseudoacacia* and to examine their structural and chemical characteristics. In addition, the study aims to evaluate the effectiveness of both the fruit-derived material and the synthesized iron oxide nanoparticles from fruit extract in removing synthetic dyes from aqueous solutions. Accordingly, this work aims to facilitate the development of a sustainable, environmentally friendly, and economically efficient remediation strategy.

RESULTS AND DISCUSSION

1. Characterization of Iron Oxide Nanoparticles

The formation of FeONPs was evaluated to determine whether the process had occurred as intended. During this assessment, the appearance of a dark, nearly black coloration was noted, and this change is generally regarded as a qualitative indication of FeONP formation [20]. Following the observation of the characteristic dark color formation, the reaction mixture was further examined by UV–Vis spectroscopy to verify nanoparticle synthesis. The most significant finding in the spectral analysis presented in Figure 1 is the substantial decrease in absorbance observed upon completion of the reaction, in comparison with the high absorption values recorded at the beginning of the experiment. This change is indicative of the fundamental chemical transformations that occur during the synthesis process. The absorbance decreased as free organic compounds bound to iron ions during FeONP formation. In particular, the absorbance variation observed in the 400–500 nm region reflects the characteristic features of FeONPs.

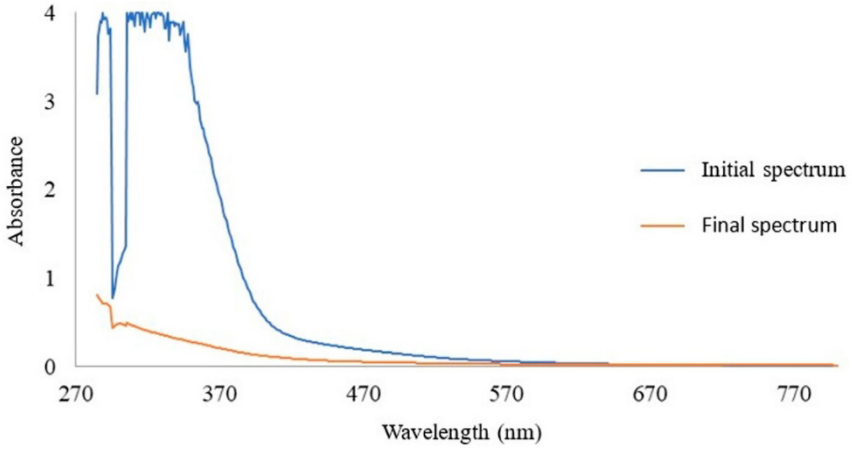

Figure 1. UV–Vis spectral variations observed during FeONP biosynthesis

The functional groups in the plant extract and the produced iron nanoparticles were determined using FTIR analysis (Figure 2). In the of 3200–3500 cm^{-1} range, a broad band was observed particularly in the extract, which is mainly attributed to O–H stretching vibrations arising from phenolic-

derived compounds; however, this band may also overlap with N–H stretching and other O–H bands in complex plant matrices [21]. In the iron nanoparticles, a slight shift and weakening the band were detected, indicating that the O–H groups interacted with iron ions and became bound to the nanoparticle surface. In the 1580–1650 cm^{-1} interval, the extract exhibited a characteristic band (≈1588 cm^{-1}) that may arise from overlapping C=C stretching, C=O stretching, or aromatic ring deformation vibrations [22]. In the present study, this band was noticeably weakened and shifted to approximately 1610 cm^{-1} following the formation of iron nanoparticles, indicating that these functional groups, particularly carbonyl and aromatic-based moieties, participated in the reduction of Fe^{3+} and the subsequent coordination of both Fe^{2+} and Fe^{3+} ions with oxygen-containing groups such as OH and conjugated C=O moieties on the nanoparticle surface [22]. In the 1000–1400 cm^{-1} interval, the extract exhibited bands mainly associated with C–N and C–O stretching vibrations, together with overlapping contributions from phenolic O–H -related modes, C–H deformation, and amine- or amide-associated NH_2 vibrations. This interpretation is consistent with previous FTIR assessments for plant-derived green synthesis [21]. In both the extract and the FeONP sample, characteristic bands were observed within the 500–800 cm^{-1} range. In the extract, two notable bands appeared at approximately 530 and 620 cm^{-1}, which fall within the typical Fe–O vibration region. In the FeONPs, this region showed additional minor features and a broader, more complex spectral profile. Similar observations reported in earlier studies suggest that the 800–400 cm^{-1} range is characteristic of Fe–O bonding, with magnetite generally exhibiting a strong Fe–O band near 573 cm^{-1} and additional shoulders attributed to surface oxidation [22]. Accordingly, the plant extract acted not only as a reducing agent, facilitating the conversion of Fe^{3+} to Fe^{2+} during nanoparticle formation, but also as a stabilizing agent through the coordination of its functional groups with the nanoparticle surface.

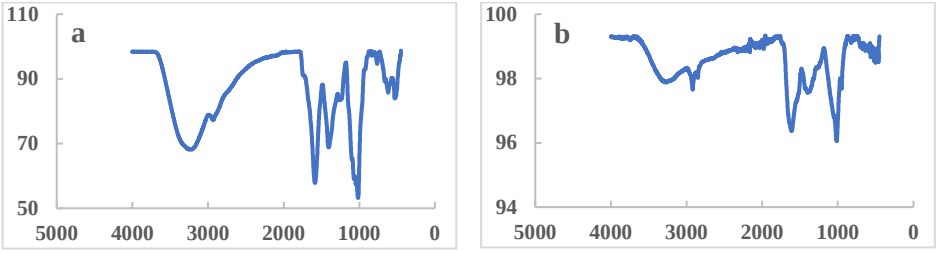

Figure 2. FT-IR spectra of the fruit extract (a) and the synthesized FeONPs (b)

The TEM images of FeNOPs synthesized from fruit extracts are presented in Figure 3. The images indicate the formation of nanoscale iron oxide particulate structures. However, due to the very small particle size and slight agglomeration, individual particle boundaries are not sharply defined. Particle size is one of the key factors influencing surface properties. Smaller particles exhibit a higher surface-to-volume ratio, enhances mass transport [23] and provides a clear advantage in the adsorption of pollutant adsorption [24]. In the present study, the high dye removal efficiencies are consistent with the formation of these very small iron oxide nanoparticles, whose large surface area supports efficient adsorption.

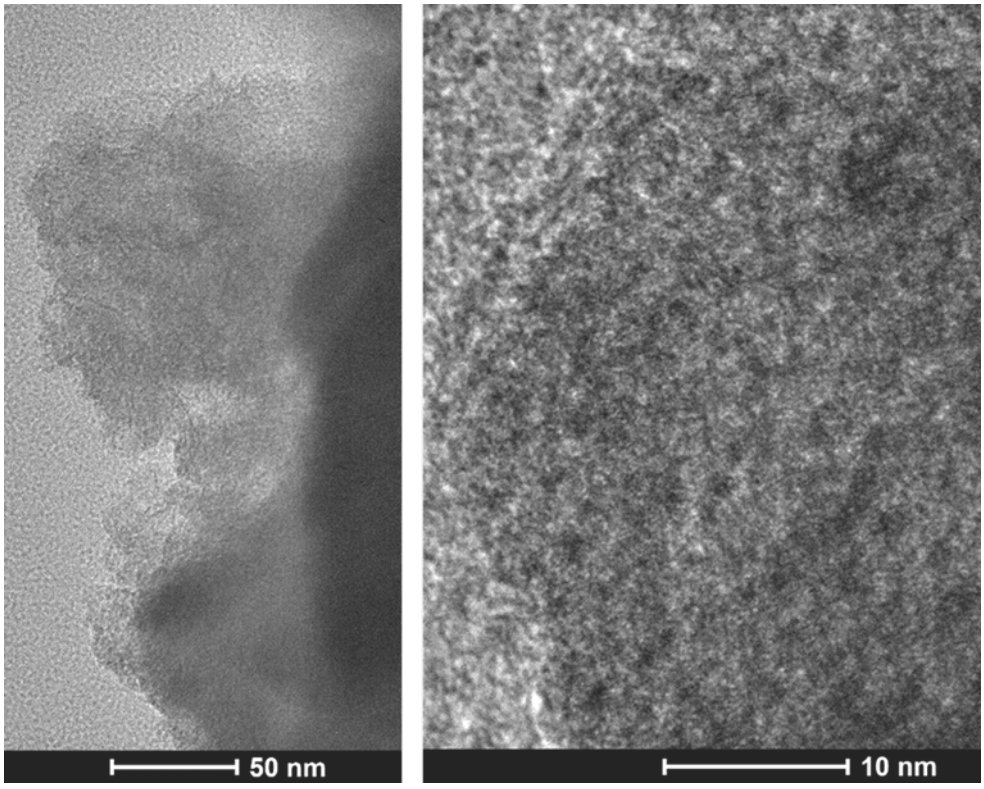

Figure 3. TEM images of FeONPs taken at different magnifications

EDX analysis confirmed the elemental composition of the produced FeONPs and their successful formation [25-26]. The EDX results for the FeONPs are presented in Figure 4 and Table 1. According to the EDX analysis, oxygen (O), carbon (C), and iron (Fe) were identified as the major elemental

constituents of the FeONPs, accounting for the highest percentage contributions. Based on the atomic percentage data, oxygen was measured at 39.32%, carbon at 25.38%, and iron at 26.34%. In the weight percentage profile, iron appeared as the dominant element with 48.81%, followed by oxygen (23.50%), copper (14.68%), and carbon (11.18%). Magnesium, silicon, and sulfur were detected only in trace quantities, with atomic percentages of 0.64%, 0.26%, and 0.94%, and corresponding weight percentages of 0.54%, 0.25%, and 1.04%, respectively. The high amounts of iron and oxygen detected in the nanoparticle samples support the presence of iron oxide in their structure [27]. Similar findings have also been reported in the literature. For example, in iron oxide nanoparticles synthesized from plant materials, the atomic percentages of iron and oxygen have been reported as follows: 33.29% Fe and 66.71% O in neem plant (*Azadirachta indica* A. Juss) leaf extract [28]; 14.21% Fe and 47.33% O in firethorn (*Pyracantha coccinea* Roem.) fruit extract [29]; 8.65% Fe and 50.55% O in algal biofilm–derived nanoparticles [30]; and 77.08% Fe and 22.97% O in nanoparticles synthesized using *Eichhornia crassipes* (Mart.) Solms leaf extract [31].

Table 1. EDX elemental composition of the FeONPs

Atom No	Element	Atomic %	Weight %
6	Carbon	25.38	11.18
8	Oxygen	39.32	23.50
12	Magnesium	0.64	0.54
14	Silicon	0.26	0.25
16	Sulfur	0.94	1.04
26	Iron	26.34	48.81
29	Copper	7.13	14.68

The identification of carbon as the third most abundant element after oxygen and iron, in both atomic and mass percentages, indicates the presence of residual organic compounds associated with the nanoparticle surface rather than being a structural component of the FeONPs. Green synthesis studies indicate that the carbon content of iron nanoparticles may vary depending on the plant species, the plant part used, and the synthesis conditions. For example, in FeONPs synthesized from mango peel extracts, carbon was reported as 14.95%, following iron (48.5%) and oxygen (34.06%) [32]; 40.79% in those produced from algal biofilms [30]; 38.46% in iron nanoparticles synthesized from *Pyracantha coccinea* Roem. fruit extract [29]; and 16.22% in nanoparticles obtained from waste tea extracts [33]. The copper signal detected in the EDX spectrum originates from the TEM copper grid used during sample preparation and does not indicate the incorporation of copper

into the nanoparticle structure [34]. The small amount of sulfur detected in the EDX analysis originates from the $FeSO_4$ precursor used in the synthesis. Similarly, Da'na [35] reported that the sulfur peak corresponds to the sulfate group derived from $FeSO_4$. The trace levels of silicon and magnesium are considered to arise from the plant extract, laboratory glassware, or minor environmental contamination during synthesis or sample preparation. These findings indicate that the FeNOPs were successfully synthesized and possess an oxidized structure.

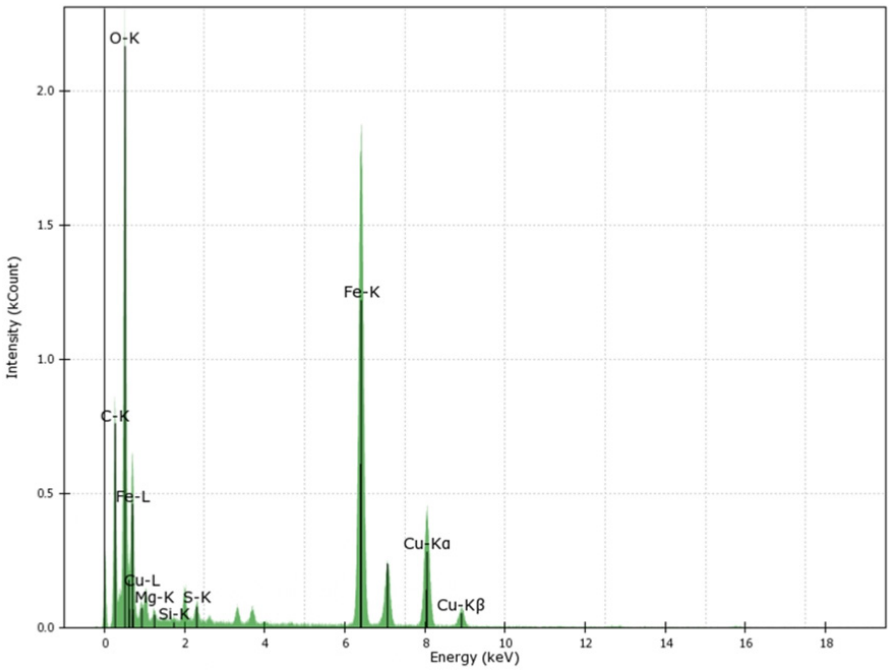

Figure 4. EDX spectra of the FeONPs

In this study, the crystal structure of iron oxide (FeOx) nanoparticles produced using *R. pseudoacacia* fruit extracts was analyzed by X-ray diffraction (XRD). The theoretical XRD peak positions reported for JCPDS Card No. 19-0629 were used as a reference for comparison, with characteristic peaks at 2θ values of 30.1° (220), 35.5° (311), 43.1° (400), 53.4° (422), 57.0° (511), and 62.6° (440). In the XRD analysis conducted in the present study, the diffraction pattern obtained is presented in Figure 5. In the 2θ regions corresponding to the theoretical peaks of JCPDS 19-0629, broad and suppressed signals were observed instead of distinct and sharp diffraction peaks. This XRD pattern

indicates a predominantly amorphous structure, with only a few weak signals that may correspond to trace crystallinity associated with iron oxide phases. In addition, the presence of broad features in the diffraction pattern, particularly at $2\theta \approx 22°$ and 36°, may also indicate the possible presence of iron oxyhydroxide phases, such as goethite (FeOOH). However, due to the absence of distinct peaks, it does not appear possible to distinguish Fe_3O_4 from other iron oxide phases such as Fe_2O_3 based on the amorphous diffraction pattern in Figure 5. For this reason, the synthesized material is described more appropriately and conservatively as iron oxide nanoparticles (FeOx) rather than being attributed to a specific crystalline phase such as Fe_3O_4. It has been reported that X-ray diffraction patterns of FeNOPs synthesized using fruit extracts tend to exhibit amorphous characteristics. For instance, in the XRD pattern of iron nanoparticles obtained from *Pyracantha coccinea* fruits, broad bands belonging to the amorphous structure were observed instead of the characteristic peaks specific to iron oxide nanoparticles [29].

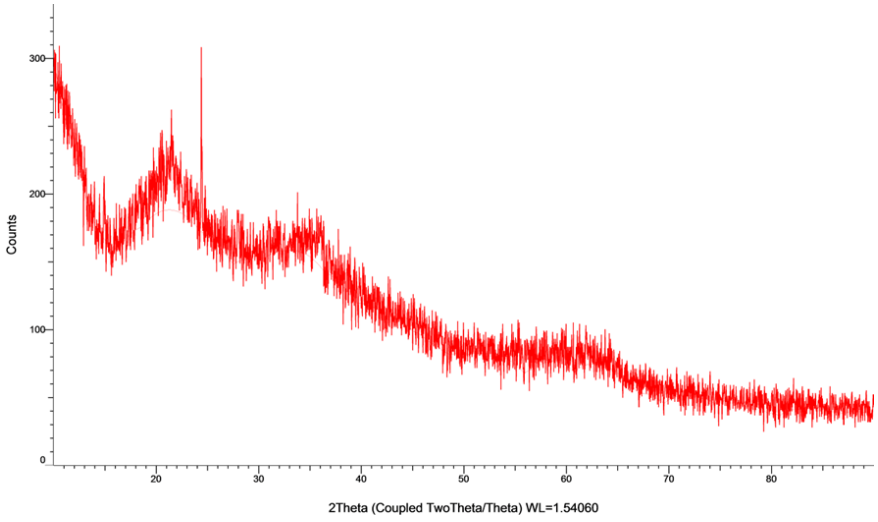

Figure 5. XRD diffraction pattern of the FeONPs

Similarly, the XRD patterns of iron nanoparticles synthesized using mango leaves, neem leaves, clove buds and rose leaves showed well-defined characteristic peaks of Fe_3O_4 together with α-Fe. However, in the nanoparticles produced using ajwain (carom) seeds, which served as the only fruit-derived source in that study, only a single weak peak was observed. This indicated a very low degree of crystallinity and the formation of a typical biosynthesized

amorphous structure due to the capping effect of biopolymers [36]. In the literature, there is evidence that iron nanoparticles synthesized not only from plant extracts derived from leaves, seeds or flowers [37-38], but also from fruit extracts, may exhibit an amorphous structure. For example, the XRD pattern of iron nanoparticles synthesized using an extract obtained from the fruit of *Dipteryx alata* Vogel displayed an amorphous character [39]. The findings suggest that crystal nucleation may be restricted due to the presence of rich biopolymer structures in the fruit extracts, which could have a negative impact on crystallization.

The amorphous structure detected in this study may be related to the presence of various biologically active components in fruit extracts, including flavonoids, phenolic acids, carbohydrates, proteins and organic acids. These compounds may participate in the reduction of iron ions and simultaneously function as surface-stabilizing agents, potentially limiting nucleus growth and hindering the complete development of a crystalline structure.

2. Dye Adsorption Studies

The residual dye concentrations in solutions at different initial methylene blue (MB) concentrations were quantified, and the percentage adsorption values were calculated for both the nanoparticle and the fruit-powder adsorbents (Figure 6A, B).

In the methylene blue (MB) adsorption experiments, the percentage adsorption values of FeONPs (1.25, 2.5, and 5.0 g/L) and fruit powder (FrP) (5.0, 10.0, and 20.0 g/L) exhibited a similar trend at low dye concentrations (2.5–40 mg/L), despite differences in adsorbent dosage. In both adsorbent substances, high adsorption efficiencies were obtained within this concentration range; adsorption reached over 97% for the FeONP, while the FrP showed values ranging from 96.4% to 99.82%. The FrP achieved almost complete removal at high adsorbent concentrations, such as 10 and 20 g/L, whereas similarly high efficiencies were obtained with the FeONPs at much lower concentrations (particularly 2.5 and 5.0 g/L). This observation is related to the higher active surface area per unit mass of the nanoparticles. At low initial concentrations, the equilibrium concentrations measured for both the FeONPs and the FrP were close to zero. The results shows that the available active surface area in the system was sufficient to completely retain the dye molecules. It also shows that increasing the amount of adsorbent provided only a limited improvement within this range. Similarly, Padmavathy et al. [40] reported that the adsorption efficiency showed only very limited variation at low initial concentrations, and that this was due to the active surface sites being

already used effectively. This result is also similar to the limited variation observed at different adsorbent concentrations in the present study; since the system did not reach surface saturation within the low concentration range, increasing the adsorbent concentration did not produce a noticeable difference in the adsorption efficiency. At moderate initial methylene blue concentrations of 100 and 250 mg/L, the lowest adsorption efficiency in the FeONP system was observed at the 1.25 g/L adsorbent concentration. At this concentration, the %Ads value was 96.61% at the 100 mg/L initial level, decreasing to 90.67% at 250 mg/L. In contrast, increasing the adsorbent concentration to 5 g/L enhanced the removal performance, yielding 94.73% adsorption at 250 mg/L. In the FrP system, at the same initial dye concentrations, the lowest value at 100 mg/L was 98.65% at 5 g/L adsorbent concentration, while the highest removal rate at 250 mg/L reached 99.63%.

The obtained results showed that by increasing the adsorbent concentration in both the FeONP and FrP systems, it is possible to maintain the adsorption capacity at moderate initial concentrations. This may be due to the increased availability of active surface sites. The result conforms with observations reported in the literature [41]. The correlation between the number of active sites and the progression of adsorption is supported by kinetic models [42]. At high initial dye concentrations (500–1000 mg/L), the amount of adsorbent used becomes the main factor affecting the adsorption performance of both the FeONP and FrP systems. In the nanoparticles, the adsorption efficiency remained at 60.68% at 500 mg/L and 55.91% at 1000 mg/L when an adsorbent amount of 1.25 g/L was used; however, increasing the amount to 5.0 g/L enhanced the efficiency to 90.26% and 93.00%, respectively. Similarly, in the FrP, the efficiency was measured as 87.47% at 500 mg/L and 67.00% at 1000 mg/L with an adsorbent amount of 5 g/L, and increasing the amount to 20 g/L improved these values to 91.08% and 75.43%, respectively. These findings indicate that, at high initial concentrations, where the amount of dye in the solution is high relative to the active surface regions, the adsorbent surface approaches saturation, and that this effect can be partially balanced by the wide surface area provided by the increased adsorbent amount. This mechanism is also consistent with the Langmuir [43] isotherm approach, which describes the tendency toward saturation in the presence of a limited number of active sites. The situation is also supported by the Q_e values. At the lowest adsorbent amounts, the Q_e values for the FeONPs reached quite high capacities, with 77.29 mg/g at an initial concentration of 100 mg/L, 181.34 mg/g at 250 mg/L, 242.74 mg/g at 500 mg/L, and 447.27 mg/g at 1000 mg/L. In contrast, in the fruit powder, the Q_e values at the lowest adsorbent amounts were lower at the same initial concentrations, occurring at 19.73 mg/g, 49.40 mg/g, 87.47 mg/g, and 134.00 mg/g, respectively. This difference arises from

the fact that the nanoparticles, due to their high specific surface area and fine morphology containing more active sites, can bind far more dye molecules per unit adsorbent [44]. When the Q_e values are taken as the basis, they provide a clear superiority compared to the fruit powder, offering 3–4 times higher adsorption capacity particularly at moderate and high initial concentrations such as 250–1000 mg/L. Comparable proportional differences were also obtained at the other adsorbent amounts.

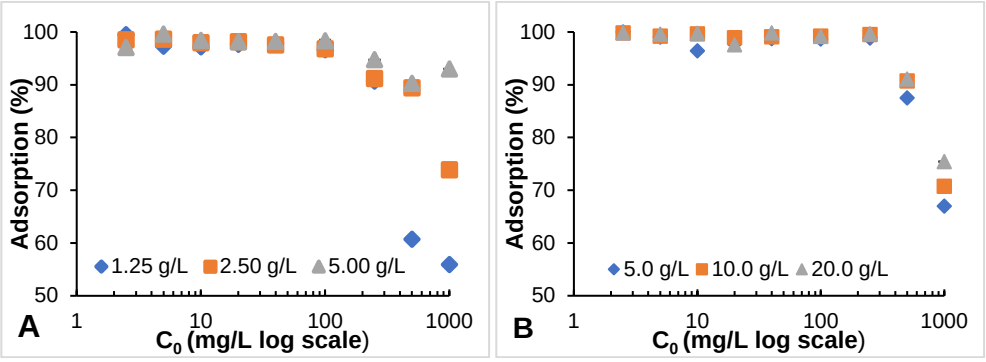

Figure 6. MB adsorption at different concentrations: (A) FeONPs, (B) FrP.

Malachite green (MG) aqueous dye solutions with various initial concentrations (2.5, 5.0, 10.0, 50.0, 100.0, and 250.0 mg/L) were exposed to three different amounts of FeONPs (1.25, 2.5, and 5 g/L) and FrP of *R. pseudoacacia* (5.0, 10.0, and 20.0 g/L) used as adsorbents for a period of 12 hours. After completion of the process, the residual dye concentration (C_e) and adsorption efficiency (% Ads.) in the solution were calculated (Figure 7A, B). In the adsorption of malachite green (MG), both FeONPs and FrP exhibited high removal efficiencies at low initial dye concentrations (2.5–10 mg/L), ranging from 94.70% to 99.99%. In this concentration range, a distinct concentration-dependent difference in performance was observed for the FrP, and the adsorption efficiency remained consistently above 99% at an adsorbent concentration of 20 g/L. These results indicate that, at low dye concentrations, both systems possess sufficient active surface sites, allowing adsorption to proceed without reaching surface saturation. As the initial concentration increased, differences in removal efficiency among the adsorbent concentrations became more noticeable. For example, at 250 mg/L MG, FeONPs achieved 90.30% removal at an adsorbent concentration of 1.25 g/L, whereas increasing the adsorbent concentration to 5 g/L enhanced the removal efficiency to 98.93%. Similarly, for the FrP, 5 g/L adsorbent provided 95.06% removal at

250 mg/L MG, while 20 g/L resulted in a markedly higher efficiency of 99.66%. These point to the fact that increasing the adsorbent concentration significantly improves the adsorption performance under high pollutant loads by increasing the overall surface area and the availability of active binding sites [42,45]. Malachite green (MG) exhibited adsorption performance similar to methylene blue (MB). The Q_e values calculated for the iron nanoparticles were higher than those of the fruit powder at all adsorbent concentrations. Furthermore, as observed for MB, the Q_e values decreased with increasing adsorbent concentration. For instance, at an initial MG concentration of 250 mg/L, the Q_e values for the iron nanoparticles were determined to be 180.60, 96.65, and 49.47 at adsorbent concentrations of 1.25, 2.50, and 5.00 g/L, respectively. In contrast, under the same conditions, the corresponding Q_e values for the fruit powder were calculated as 47.53, 24.34, and 12.46, respectively. At low adsorbent concentrations, the dye molecules present in the solution are required to bind to a limited density of active surface sites. Therefore, a larger amount of dye is adsorbed per unit mass of the adsorbent. As the adsorbent concentration increases, the dye molecules have access to a larger surface area; however, since the total amount of dye in the solution remains constant, some of the available active sites remain unused. Consequently, less dye is adsorbed per unit mass of the adsorbent, resulting in lower Q_e values.

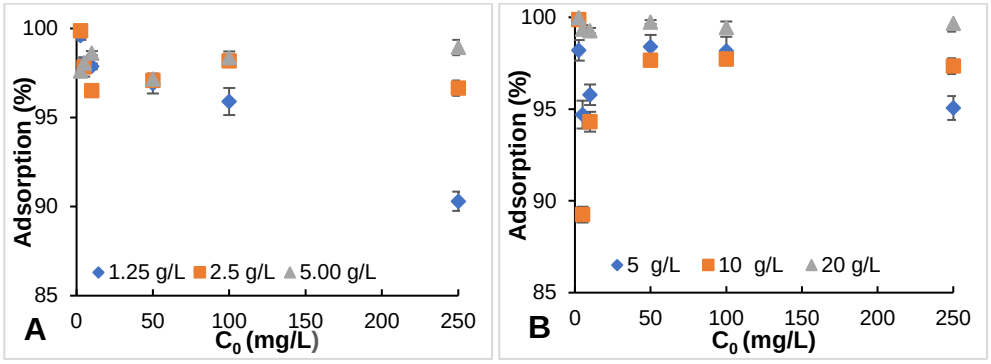

Figure 7. MG adsorption at different concentrations: (A) FeONPs, (B) FrP.

In the removal of another dye, phenol red (PR), adsorption tests were carried out with solutions at initial concentrations ranging from C_0 = 2.50 to 250.00 mg/L and FeONP adsorbent concentrations of 1.50, 2.00, and 5.00 g/L. The adsorption performance was evaluated in terms of equilibrium concentrations (C_e) and % adsorption (Figure 8A, B).

At an initial dye concentration of 2.5 mg/L, methylene blue (MB) and malachite green (MG) exhibited high removal efficiencies in the range of 95–99% using fruit-derived FeONPs at an adsorbent dose of 1.25 g/L, whereas phenol red (PR) showed a comparatively limited adsorption performance of 89.38% even at a higher FeONP dose of 1.50 g/L at the same initial concentration. However, while holding the initial dye concentration (2.5 mg/L) constant, increasing the adsorbent amount to 2.00 and 5.00 g/L resulted in a substantial enhancement of PR removal, with efficiencies reaching 98.81% and 98.87%, respectively. These findings suggest that PR adsorption is more sensitive to the amount of adsorbent at low levels than the other dyes, and that high removal efficiencies are attainable only when an adequate surface area is available. When the dye concentration ranged between 5 and 250 mg/L, a gradual decrease in PR removal efficiency was observed at an adsorbent amount of 1.50 g/L. At an adsorbent amount of 1.50 g/L, the adsorption efficiency was 86.93% at 5 mg/L and progressively declined with increasing concentration, reaching 68.81% at 250 mg/L. Similarly, at an adsorbent amount of 2.00 g/L, PR removal efficiency generally decreased with increasing initial dye concentration, declining from 89.24% at 5 mg/L to 82.46% at 250 mg/L. In contrast, at an adsorbent amount of 5.00 g/L, the system exhibited enhanced stability against increasing dye concentration, maintaining efficiencies above 91.50% up to 100 mg/L before decreasing to 83.67% at 250 mg/L. These results indicate that, particularly at lower adsorbent amounts, increasing the initial dye concentration facilitates surface saturation, whereas at higher adsorbent amounts this effect is partially offset by the increased availability of active surface area. By contrast, at a low initial PR dye concentration (C_0 = 2.5 mg/L), removal efficiencies above 95% were achieved nearly at all adsorbent amounts, except for the lowest FeONP dose (1.50 g/L), indicating that surface saturation was not reached under low adsorbate-to-adsorbent ratio conditions. It was observed that increasing the initial concentration generally led to a decrease in removal efficiency. In particular, for the FrP, at an adsorbent amount of 10 g/L, the lower removal values observed at initial concentrations of 5 and 10 mg/L (35.64% and 18.94%, respectively) deviated from the general concentration–efficiency relationship. However, the systematic decreasing trend was preserved in the other dose and concentration combinations. For example, at an initial concentration of 100 mg/L, the removal efficiencies at 5, 10, and 20 g/L were determined as 57.87%, 76.94%, and 58.94%, respectively; when the initial concentration was increased to 250 mg/L, these values decreased to 20.25%, 35.02%, and 51.53%. These results indicate that increasing dye concentration limits removal performance at all doses, and that although increasing the adsorbent dose at higher concentrations provides a partial improvement, the efficiency levels observed at lower concentrations could not be achieved.

The Q_e values calculated for phenol red were higher for the FeONP adsorbent than for the FrP, similar to the results obtained for the other two dyes examined in this study. Furthermore, a systematic decrease in Q_e values was observed with increasing adsorbent dosage. The Q_e values calculated for an initial dye concentration of 250 mg/L and FeONP adsorbent concentrations of 1.5, 2.0 and 5.0 g/L were found to be 114.69, 103.07 and 41.83 mg/g respectively. At the same initial dye concentration, the Q_e values for the FrP at adsorbent dosages of 5.0, 10.0, and 20.0 g/L were 10.13, 8.75, and 6.44 mg/g. The decrease in Q_e values observed with increasing adsorbent concentration, as noted for the other dyes, can be explained by reduction in adsorption capacity per unit mass resulting from the increase in adsorbent amount at a fixed initial concentration.

When the adsorption capacities (Q_e) are considered, the overall performance of the dyes followed the order MB> MG > PR. These results can be partly explained by the chemical structures of the dye molecules and the possible influence of solution pH on the adsorption process. The natural pH values of the dye solutions used in the study were measured and determined as 4.88 for MB, 3.02 for MG, and 3.76 for PR. The relatively less acidic pH of the MB solution could be one of the factors influencing its higher observed adsorption efficiency. However, no pH-controlled experiments were performed. Under such pH conditions, the adsorbent surface may become more negatively charged, which may enhance electrostatic attraction toward cationic dyes. Similarly, higher pH values increase the negative charge on the adsorbent surface and favor the adsorption of positively charged molecules [46]. In addition, the pH-dependent protonation of nitrogen and sulfur groups may modulate dye–surface interactions; under acidic conditions, their protonated forms can also contribute to adsorption through electrostatic attraction and hydrogen bonding [47]. The relatively lower adsorption performance of MG and PR may be associated with differences in their molecular structures and their behavior under the studied solution conditions.

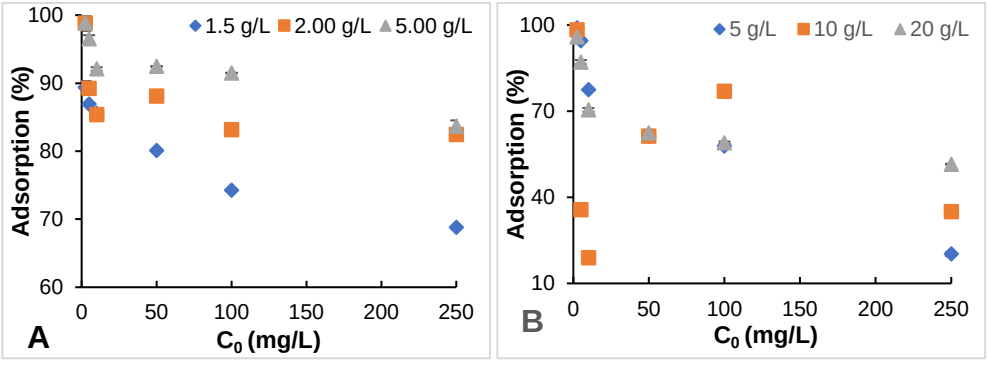

Figure 8. PR adsorption at different concentrations: (A) FeONPs, (B) FrP.

CONCLUSION

Iron oxide nanoparticles (FeONPs) were produced through green synthesis using *R. pseudoacacia* fruit extract and investigated by UV–Vis, XRD, FTIR, TEM, and EDX techniques. The obtained data indicated the successful synthesis of amorphous FeONPs with particle sizes in the nanoscale range. The adsorption performance of synthesized FeONPs and FrP was comparatively investigated for malachite green (MG), phenol red (PR), and methylene blue (MB). The results of the study showed that the adsorption capacity ranking was MB > MG > PR. FeONPs exhibited higher Q_e values in all dye systems in comparison to fruit powder. Efficient removal of the dye was observed at low and medium initial concentrations, with an increase in the amount of adsorbent resulting in an enhancement of the total removal process. However, this was associated with a reduction in the adsorption capacity per unit mass. Biosynthesized FeONP may serve as a sustainable, economical, and efficient adsorbent for dye removal, thereby representing a significant alternative in advanced environmental treatment technologies.

EXPERIMENTAL SECTION

1. Sampling

The fruits of *R. pseudoacacia* trees cultivated for landscaping purposes in the Eskibağlar Neighborhood of Gümüşhane Province, Türkiye, were collected in September 2023.

2. Preparation of Fruit Extracts

The fruits of the plant were dried at room temperature in an environment protected from sunlight and subsequently pulverized into a fine powder with a blender. The entire fruit (legume pod), including both the pericarp and the enclosed seeds, was used without any prior separation. A total of 1.1 kg of this powder was transferred into a 20-L container along with 10 L of distilled water. The mixture was boiled in a closed vessel for 2.5 hours and then allowed to cool to room temperature. After the formation of the extract, the mixture was separated using sieves with pore sizes of 1.00, 0.50, and 0.25 mm. The dry matter content of the resulting extract was then determined to be 4.00% ± 0.25 using a digital refractometer (Hanna HI96801). The extract was concentrated in a vacuum evaporator at 60 °C and 150 mbar to obtain a dry matter content of 10% [29].

3. Synthesis of Iron Oxide Nanoparticles (FeONPs)

For the green synthesis of FeONPs from *R. pseudoacacia* fruit samples, solutions containing iron(III) and iron(II) ions were prepared. For this purpose, 125 mL of a 0.2 M Fe^{3+} solution was prepared using $FeCl_3 \cdot 6H_2O$ salt. Additionally, 3.8 g of $FeSO_4$ was weighed to obtain 125 mL of a 0.1 M Fe^{2+} solution, and both substances were dissolved separately in beakers and then combined in a volumetric flask and made up to 250 mL. Then, 250 mL of *R. pseudoacacia* fruit extract (FE) with a 10% dry matter content was added to a 600-mL beaker. Using a pH meter (OHAUS Starter 3000), The pH value was then adjusted to 10 by gradually dropping 1.0 M NaOH into the solution. Following this, the solution was stirred on a magnetic stirrer (750 rpm), and the Fe^{2+}/Fe^{3+} solution was added dropwise at a rate of one drop per second using a separatory funnel. This dropwise addition was completed in 60 minutes for the total volume of 250 mL. Then, the beaker was covered with a glass lid and stirred at 750 rpm for 2.5 hours [48-49]. The synthesis of FeONP was accompanied by a visible change in color of the reaction mixture, giving it a completely black appearance. The resulting FeONP solution was pipetted into eight 50 mL falcon centrifuge tubes and centrifuged at 4000 rpm using a NÜVE NF 800R centrifuge and this process was repeated three times. The precipitates were placed in pre-weighed glass Petri dishes and air-dried in a vacuum dryer at 60 °C for three hours, thereby completing the synthesis process [48-49].

4. Characterization of Iron Oxide Nanoparticles

UV–Vis spectroscopy was used to confirm the formation of FeONPs using a Shimadzu UV-1800 spectrophotometer (Kyoto, Japan) within the wavelength range of 200–800 nm. To evaluate the chemical structure of the nanoparticles obtained from the *R. pseudoacacia* fruit extract (FE), Fourier Transform Infrared Spectroscopy (FTIR) analysis was performed on both the nanoparticles and the plant extract used in the synthesis. The analyses were performed using a PerkinElmer FT-IR spectrophotometer (model: UATR Two) at the Gümüşhane University Central Research Laboratory Application and Research Center, within the wavenumber range of 4000–450 cm^{-1}.

Structural characterization of the FeONPs was performed using X-ray diffraction (XRD). The measurements were performed using a Bruker D8 DISCOVER instrument at the Bayburt University Central Research Laboratory. A copper (Cu) anode served as the X-ray source, operated at 40 kV and 40 mA. Diffraction patterns were recorded over the 2θ range of 10°–80°.

The morphological and elemental characteristics of the synthesized FeONPs were examined using a transmission electron microscope (TEM) at

the Bayburt University Central Research Laboratory. The analyses were carried out with a Thermo Fisher Scientific Talos F200S TEM operated at 200 kV. Elemental composition was determined using an energy-dispersive X-ray spectroscopy (EDX) system attached to the TEM. The scale bars in the TEM images were generated by the instrument software.

5. Adsorption of Dyes

Green-synthesized FeONPs and *R. pseudoacacia* fruit powder (FrP) were used, and stock solutions of each dye (malachite green, MG; methylene blue, MB and phenol red, PR) were prepared at a concentration of 2500.0 mg/L. From these stock solutions, defined volumes were taken and diluted with deionized water to obtain seven different dye solutions at concentrations of 2.5, 5.0, 10.0, 20.0, 40.0, 100.0 and 250.0 mg/L for MG and PR, and nine solutions for MB by additionally preparing 500.0 and 1000.0 mg/L concentrations. The original pH values of each prepared dye solution (MB at pH 4.88, MG at pH 3.02, and PR at pH 3.76) were measured. To perform the adsorption tests, 0.0125, 0.025 and 0.050 g of FeONPs were placed into polypropylene (PP) tubes, to which 10 mL of the dye solutions were added. Accordingly, the concentrations of the adsorbent suspensions were set to 1.25, 2.50 and 5.00 g/L. Then, blank sampling was carried out by adding 10 mL of deionized water to 0.050 g and 0.100 g of FeONPs. For phenol red (PR), preliminary trials showed that the lowest FeONP suspension concentration (1.25 g/L) resulted in insufficient dye removal; therefore, slightly higher doses (1.50 and 2.00 g/L), in addition to 5.00 g/L, were adopted to ensure measurable adsorption. For FrP, higher adsorbent doses (5, 10 and 20 g/L) were employed because the powdered *R. pseudoacacia* fruits exhibited noticeably lower adsorption capacity compared with the FeONPs. The samples were shaken on an orbital shaker at 50 rpm for 12 h and then centrifuged at 5000 rpm for 15 min to separate the solid and liquid phases. The residual dye concentrations in the supernatants obtained after centrifugation were analyzed using a UV–Vis spectrophotometer [30,50]. The spectral profile of methylene blue was evaluated by scanning a 5.0 mg/L solution between 200 and 1000 nm using the spectrophotometer, which clearly showed a distinct absorption maximum at 664 nm. For quantitative calibration, standard solutions prepared at 1.0, 2.5, 5.0, 10.0 and 25.0 mg/L were analyzed, and the resulting measurements were used to generate a linear calibration curve described by $y = 0.1477x + 0.0422$, with an R^2 value of 0.999. In addition to the measurements reported for methylene blue, the same wavelength-scanning and calibration procedure was applied to malachite green and phenol red. Malachite green displayed its absorption maximum at 617 nm, and the calibration curve obtained from its standard solutions was described by $y = 0.353x - 0.0114$

(R^2 = 0.998). Phenol red exhibited a maximum absorbance at 430 nm, with a corresponding calibration relationship expressed as y = 0.0248x − 0.0038. In this study, the residual dye concentration in the solution (C_e) was determined from the UV–Vis absorbance data for the calculation of dye adsorption onto FeONPs. Adsorption efficiency (%) and adsorption capacity per unit mass of adsorbent (Q_e, mg/g) were calculated. All tests were repeated at least three times, and the results are reported as mean ± standard deviation. All necessary calculations were carried out using the formulas presented below (Equations 1–3) [30,50].

$$Remaining\ dye\ \left(\frac{mg}{L}\right) = (A - B)/E \quad (1)$$

Equation 1 defines A as the recorded signal intensity, with B serving as the intercept and E representing the slope of the calibration graph. The % adsorption was determined using Equation 2.

$$Adsorption\ Percentage = ((C_0 - C_e)/C_0)\ x\ 100 \quad (2)$$

According to Equation 2, C_0 (mg/L) refers to the initial dye level, while Ce (mg/L) indicates the residual concentration in the equilibrium phase. Using the dye concentration remaining in the solution phase (C_e), the amount of dye taken up by 1 g of FeONP (mg/g) was determined according to Equation 3.

$$Q_e = ((C_0 - C_e)\ x\ V)/m \quad (3)$$

In Equation 3, V represents the volume of the adsorbate solution (L), m indicates the mass of the adsorbent (g), Q_e denotes the amount of adsorbate adsorbed per gram of FeONPs (mg/g), C_0 refers to the initial dye concentration (mg/L), and C_e represents the equilibrium dye concentration (mg/L).

REFERENCES

1. Alengebawy, A.; Abdelkhalek, S. T.; Qureshi, S. R.; Wang, M. Q. *Toxics* **2021**, 9 (3), 42.
2. Kumar, A.; Bisht, B. S.; Joshi, V. D.; Dhewa, T. *Int. J. Environ. Sci.* **2011**, 1 (6), 1079–1093.
3. Çınar Acar, B.; Yüksekdağ, Z. *OKU J. Inst. Sci. Technol.* **2023**, 6 (1), 1006–1029.
4. Tziourrou, P.; Golia, E. E. Soil Syst. 2025, 9 (4), 137.
5. Beni, A. A.; Jabbari, H. Results Eng. 2022, 15, 100467.
6. Kulkarni, A. G.; De Britto, S.; Jogaiah, S. Economic considerations and limitations of green synthesis vs chemical synthesis of nanomaterials. In *Advances in Nano-fertilizers and Nano-pesticides in Agriculture*; Woodhead Publishing: Cambridge, UK, **2021**; pp. 459–468.

7. Mutaf, T.; Çalışkan, G.; Öncel, S. Ş.; Elibol, M. *Ege J. Fish. Aquat. Sci.* **2023**, 40 (1), 81–89.
8. Ying, S.; Guan, Z.; Ofoegbu, P. C.; Clubb, P.; Rico, C.; He, F.; Hong, J. *Environ. Technol. Innov.* **2022**, 26, 102336.
9. Hussain, A.; Lakhan, M. N.; Hanan, A.; Soomro, I. A.; Ahmed, M.; Bibi, F.; Zehra, I. *Mater. Today Sustain.* **2023**, 100420.
10. Akar, B.; Baltacı, C.; Düzgün, A. Ö.; Karpuz, O.; Karakullukcu, V.; Erdoğdu, E. G. *Environ. Eng. Manag. J.* **2025**, 24 (5), 1013–1025.
11. Yakut, Ş. M.; Karataş, M. *Duzce Univ. J. Sci. Technol.* **2021**, 9, 1267–1281.
12. Bukhari, A.; Ijaz, I.; Gilani, E.; Nazir, A.; Zain, H.; Saeed, R.; Naseer, Y. Coatings 2021, 11 (11), 1374.
13. Coelho, L. M.; Rezende, H. C.; Coelho, L. M.; de Sousa, P. A.; Melo, D. F.; Coelho, M. N. Bioremediation of polluted waters using microorganisms. In *Advances in Bioremediation of Wastewater and Polluted Soil*; IntechOpen: Rijeka, Croatia, **2015**; Vol. 10, pp. 2–15.
14. Ihsanullah, I.; Jamal, A.; Ilyas, M.; Zubair, M.; Khan, G.; Atieh, M. A. *J. Water Process Eng.* **2020**, 38, 101680.
15. Mihai, S.; Bondarev, A.; Necula, M. *Processes* **2025**, 13 (2), 589.
16. Arslan, E. S. *Turk. J. For.* **2019**, 20 (2), 142–148.
17. Marinas, I. C.; Oprea, E.; Geana, E. I.; Chifiriuc, C.; Lazar, V. *J. Serb. Chem. Soc.* **2014**, 79 (11), 1363–1378.
18. Hosseinihashemi, S. K.; HosseinAshrafi, S. K.; Goldeh, A. J.; Salem, M. Z. *BioResources* **2016**, 11 (1), 1634–1646.
19. Aktürk, B. K.; Arslan Burnaz, N. *Chem. Biodivers.* **2025**, e00547.
20. Aydogan, T.; Dumanlı, F. T. Ş.; Derun, E. M. *J. Polytech.* **2022**, 25 (4), 1423–1427.
21. Pasieczna-Patkowska, S.; Cichy, M.; Flieger, J. *Molecules* **2025**, 30 (3), 684.
22. Abdullah, J. A. A.; Eddine, L. S.; Abderrhmane, B.; Alonso-González, M.; Guerrero, A.; Romero, A. *Sustain. Chem. Pharm.* **2020**, 17, 100280.
23. Losito, D. W.; Souza, N. I.; Martins, T. S.; Britos, T. N.; Schumacher, M. L.; Haddad, P. S. *J. Mater. Sci.* **2024**, 59 (34), 16038–16068.
24. Doan, L. *ChemEngineering* **2023**, 7 (5), 77.
25. Hussain, M.; Ceccarelli, R.; Marchisio, D. L.; Fino, D.; Russo, N.; Geobaldo, F. *Chem. Eng. J.* **2010**, 157 (1), 45–51.
26. Titus, D.; Samuel, E. J. J.; Roopan, S. M. Nanoparticle characterization techniques. In *Green Synthesis, Characterization and Applications of Nanoparticles*; Shukla, A. K.; Iravani, S., Eds.; Elsevier: Amsterdam, Netherlands, **2019**; pp. 303–319.
27. Winsett, J.; Moilanen, A.; Paudel, K.; Kamali, S.; Ding, K.; Cribb, W.; Neupane, S. *SN Appl. Sci.* **2019**, 1, 1–8.
28. Zambri, N. D. S.; Taib, N. I.; Abdul Latif, F.; Mohamed, Z. *Molecules* **2019**, 24 (20), 3803.
29. Karakullukçu, V.; Akar, B.; Baltacı, C.; Düzgün, A. Ö.; Karpuz, Ö. *Karaelmas Sci. Eng. J.* **2023**, 13 (2), 255–265.

30. Demirel, İ. T.; Akar, B.; Baltacı, C.; Karpuz, Ö.; Gülbahar, E. *J. Anatolian Environ. Anim. Sci.* **2024**, 9 (2), 174–183.
31. Jagathesan, G.; Rajiv, P. *Biocatal. Agric. Biotechnol.* **2018**, 13, 90–94.
32. Desalegn, B.; Megharaj, M.; Chen, Z.; Naidu, R. *Heliyon* **2019**, 5 (5).
33. Gautam, A.; Rawat, S.; Verma, L.; Singh, J.; Sikarwar, S.; Yadav, B. C.; Kalamdhad, A. S. *Environ. Nanotechnol. Monit. Manag.* **2018**, 10, 377–387.
34. Król-Gracz, A.; Michalak, E.; Nowak, P.; Dyonizy, A. *Open Chem.* **2011**, 9 (6), 982–989.
35. Da'na, E.; Taha, A.; Afkar, E. *Appl. Sci.* **2018**, 8 (10), 1922.
36. Afsheen, S.; Tahir, M. B.; Iqbal, T.; Liaqat, A.; Abrar, M. *J. Alloys Compd.* **2018**, 732, 935–944.
37. Kouhbanani, M. A. J.; Beheshtkhoo, N.; Taghizadeh, S.; Amani, A. M.; Alimardani, V. *Adv. Nat. Sci.: Nanosci. Nanotechnol.* **2019**, 10 (1), 015007.
38. Góral-Kowalczyk, M.; Grządka, E.; Orzeł, J.; Góral, D.; Skrzypek, T.; Kobus, Z.; Nawrocka, A. *Materials* **2024**, 17 (11), 2515.
39. Corrêa, C. R. R.; de Siqueira, A. B.; Matos Lopes, P. R.; Ambrosio, J. A. R.; Simioni, A. R.; de Vasconcelos, L. G.; Morais, E. B. *AQUA—Water Infrastruct. Ecosyst. Soc.* **2024**, 73 (4), 771–789.
40. Padmavathy, K. S.; Madhu, G.; Haseena, P. V. *Procedia Technol.* **2016**, 24, 585–594.
41. Vargas, A. M. M.; Cazetta, A. L.; Kunita, M. H.; Silva, T. L.; Almeida, V. C. *Chem. Eng. J.* **2011**, 168 (2), 722–730.
42. Ho, Y. S.; McKay, G. *Process Biochem.* **1999**, 34 (5), 451–465.
43. Langmuir, I. *J. Am. Chem. Soc.* **1918**, 40 (9), 1361–1403.
44. Mansour, A. T.; Alprol, A. E.; Ashour, M.; Ramadan, K. M.; Alhajji, A. H.; Abualnaja, K. M. *Gels* **2022**, 8 (5), 310.
45. Foo, K. Y.; Hameed, B. H. *Chem. Eng. J.* **2010**, 156 (1), 2–10.
46. Galloni, M. G.; Bortolotto, V.; Falletta, E.; Bianchi, C. L. *Polymers* **2022**, 14 (22), 4897.
47. Aziz, D. M.; Hassan, S. A.; Aziz, S. B.; Kader, D. A. *Next Mater.* **2025**, 9, 101015.
48. Yusefi, M.; Shameli, K.; Ali, R. R.; Pang, S. W.; Teow, S. Y. *J. Mol. Struct.* **2020**, 1204, 127539.
49. Gedikli, H.; Akdogan, A.; Karpuz, O.; Akmese, O.; Kobya, H. N.; Baltaci, C. *BioResources* **2024**, 19 (1), 380.
50. Bozbeyoglu, P.; Duran, C.; Baltaci, C.; Gundogdu, A. *Hittite J. Sci. Eng.* **2020**, 7 (3), 239–256.